
Proceedings Paper:
Rigby, S. orcid.org/0000-0001-6844-3797, Mendham, E., Farrimond, D. orcid.org/0000-0002-9440-4369 et al. (3 more authors) (2024) Re-visiting the secondary shock. In: Proceedings of The 19th International Symposium on Interaction of the Effects of Munitions with Structures (ISIEMS 19). 19th International Symposium on Interaction of the Effects of Munitions with Structures (ISIEMS), 09-13 Dec 2024, Bonn, Germany. International Symposium on Interaction of the Effects of Munitions with Structures (ISIEMS)

Distribution: For public release

Re-visiting the Secondary Shock

SE Rigby[1,2*], E Mendham[1], DG Farrimond[1,3], A Tyas[1,3], EG Pickering[4], G Pezzola[5]

School of Mechanical, Aerospace and Civil Engineering, University of Sheffield, S1 3JD, UK

1 University of Sheffield, UK
2 Arup, UK
3 Blastech Ltd., UK
4 Cranfield University, UK
5 US Army ERDC, USA
*sam.rigby@sheffield.ac.uk

Keywords: Blast loading, Empirical method, Secondary Shock, Small-scale testing

Abstract

The secondary shock, caused by collapse and re-expansion of an inward-facing shock originating at the edge of the fireball, is a regular feature in blast trials data and the output from numerical models. It has also been postulated that, since the secondary shock travels through the detonation products, it contains important information about the state of the explosive gasses shortly after detonation. Despite this, the secondary shock is often overlooked, and there is, as yet, no established method for predicting its form and magnitude. The current authors recently developed such a method, based on superposition of the UFC positive and negative phase loading from the original charge mass, plus an additional positive phase modelled using a smaller charge at some fraction of the original charge mass (at the same distance). This "dummy charge mass" has been calibrated from 76 experimental tests using 180–350g of PE4, PE8, and PE10 plastic explosives, and is typically around 4–5% of the original charge mass. This paper provides an overview of the method and introduces new data from smaller scale testing (1–3g PE10), as well as additional diagnostics such as high speed video.

Introduction

After an explosive detonates, the resulting high pressure detonation products begin to expand at supersonic velocities, compressing the surrounding air into a shock wave. This compressed air arrests the flow of the detonation product cloud (DPC) until it eventually over-expands and its velocity decreases until an inward-travelling shock is formed. This shock converges at the centre of the charge and is reflected outwards, passing back through the DPC and eventually breaking out into the air, forming the well-known secondary shock which trails the primary shock and generally arrives between the end of the positive phase and the minimum of the negative phase [1]. The secondary shock is regularly observed in experimental blast pressure histories [2], and can be readily seen in high speed video footage of explosions [3].

The motivation for the current work is three-fold:

1. Structural elements such as masonry walls [4], glazing [5], cable-nets and other types of flexible façade [6] are known to be sensitive to the exact form and magnitude of the negative phase.
2. Large-scale industrial incidents (such as the 2020 Beirut explosion [7]) may produce loads with a secondary shock component that is comparable to or even exceeding the magnitude of the primary shock from more conventional-sized explosions.
3. Because the secondary shock travels through the DPC in the early stages, its properties are intrinsically linked to the pressure-volume-energy state of the explosive products. In particular, the delay between the primary and secondary shock arrival times may be used to infer sonic velocity in the DPC [8]. Clearly, better understanding of the secondary shock will lead to an improved understanding of, and an enhanced ability to derive, properties of explosives.

Despite some previous efforts to develop secondary shock arrival time predictions as a function of basic explosive parameters [9], or using the secondary shock to calibrate equation of state parameters through numerical modelling [10], the secondary shock has otherwise received little attention.

This paper presents an overview of a new method for predicting the secondary shock [11] based on summation of the loading from the original charge mass (W), plus the contribution of a secondary loading pulse from a smaller explosive mass (cW). The model has two parameters: charge mass multiplier, c, which is used to derive the smaller ("dummy") charge mass, and scaled time delay, dt_{lag} which is used to make adjustments to secondary shock arrival time. These parameters have previously been derived from 76 experimental tests using 180–350g of PE4, PE8, and PE10 plastic explosives, originally reported in Ref. [12]. In this work, the method is extended to incorporate test data from smaller-scale tests using 1–3g PE10, originally reported in Ref. [13].

Experimental Work

The small-scale testing arena at the University of Sheffield Blast & Impact Laboratory, shown in Figure 1(a), was used to perform 32 tests, from which 41 datapoints were recorded. Two concrete blockwork walls were erected 2.28 m apart on a flat, reinforced concrete slab. The surfaces of the blockwork walls which were facing each other were clad with thin steel plates to ensure a smooth reflecting surface, and to provide threaded holes through which to affix the pressure sensors (inserted from behind via access holes drilled through the walls).

A combination of Kulite HKM-375 and StrainSense XPM-5 piezo-resistive pressure gauges were employed in this testing, which were located at approximately 10 mm above the ground slab, directly in line with the centre of a shallow channel which had been cut through the concrete pad. This channel was filled with sand, and was used to run the breakwire and detonator cabling through, to ensure there were no obstructions in the vicinity of the charge.

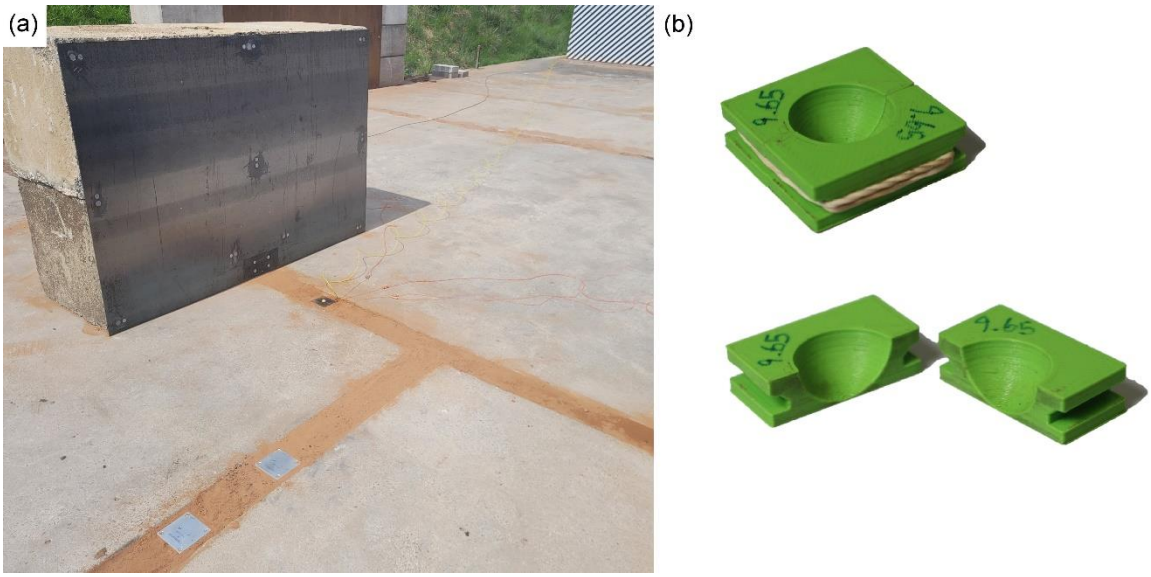

Figure 1. (a) Photograph of the small-scale test arena with 3 g PE10 hemispherical charge visible at 0.456 m stand-off distance from reflecting wall, with flush-mounted pressure gauge at bottom-centre [note: second reflecting wall out of shot on the right hand side, positioned central to the sand channel]. (b) Bespoke 3D-printed charge moulds.

3 g and 1 g hemispherical PE10 charges (86% PETN, 14% binder-plasticizer) were formed using bespoke 3D-printed charge moulds, see Figure 1(b), and were sat in the middle of a small steel plate with a pre-formed hole through the centre. The detonators (Euronel non-electrical, 0.8 g TNT-equivalent NEQ) were placed through this hole from beneath, ensuring the charges could be considered to be centrally detonated. Recordings were triggered off the breakwire signal (the breakwire itself was wrapped around the detonator) using a 16-bit digital oscilloscope and TiePie software, with a typical sampling rate of 312.5 kHz at 16-bit resolution. For the 3 g tests, pressure was recorded at both walls with the charge placed some distance between the two, providing datapoints at pairs of stand-off distances (0.456 m and 1.824 m, etc.), whereas in the 1 g tests tests the second wall was replaced with smaller obstacles to study the effects of clearing. Results from these tests are omitted here for brevity. Charges were measured using scales accurate to ±1 mg.

Table 1. Summary of the experimental datasets. Scaled distance calculated assuming a TNT equivalence of 1.22 for PE10 [12] and a detonator NEQ of 0.8 g_{TNT}

Stand-off, R (m)	PE10 charge mass, W (g)	TNT-equivalent charge mass, W (g_{TNT})	Scaled distance, Z ($m/kg_{TNT}^{1/3}$)	No. data points	Source
0.941	1	2.02	7.44	11	[13]
0.456	3	4.46	2.77	5	
0.684			4.16	5	
0.912			5.54	5	
1.368			8.31	5	
1.596			9.70	5	
1.824			11.08	5	
2.000	250	305.8	2.97	3	[12]
3.000			4.45	4	
4.000			5.94	4	
5.000			7.42	4	
6.000			8.91	4	
7.000			10.39	4	
8.000			11.87	2	
			Total:	66	

The test methodology for the 250 g charges was essentially the same, albeit at larger scales. Inclusion of this data brings the total number of datapoints to 66, although to reiterate only the 1 g and 3 g data are used herein to derive parameters for the new predictive model (since the 250 g tests were previously used to derive the model in Ref. [11]). A summary of the experiments is provided in Table 1, and measured secondary shock parameters for the 1 g and 3 g tests are shown in Figure 2.

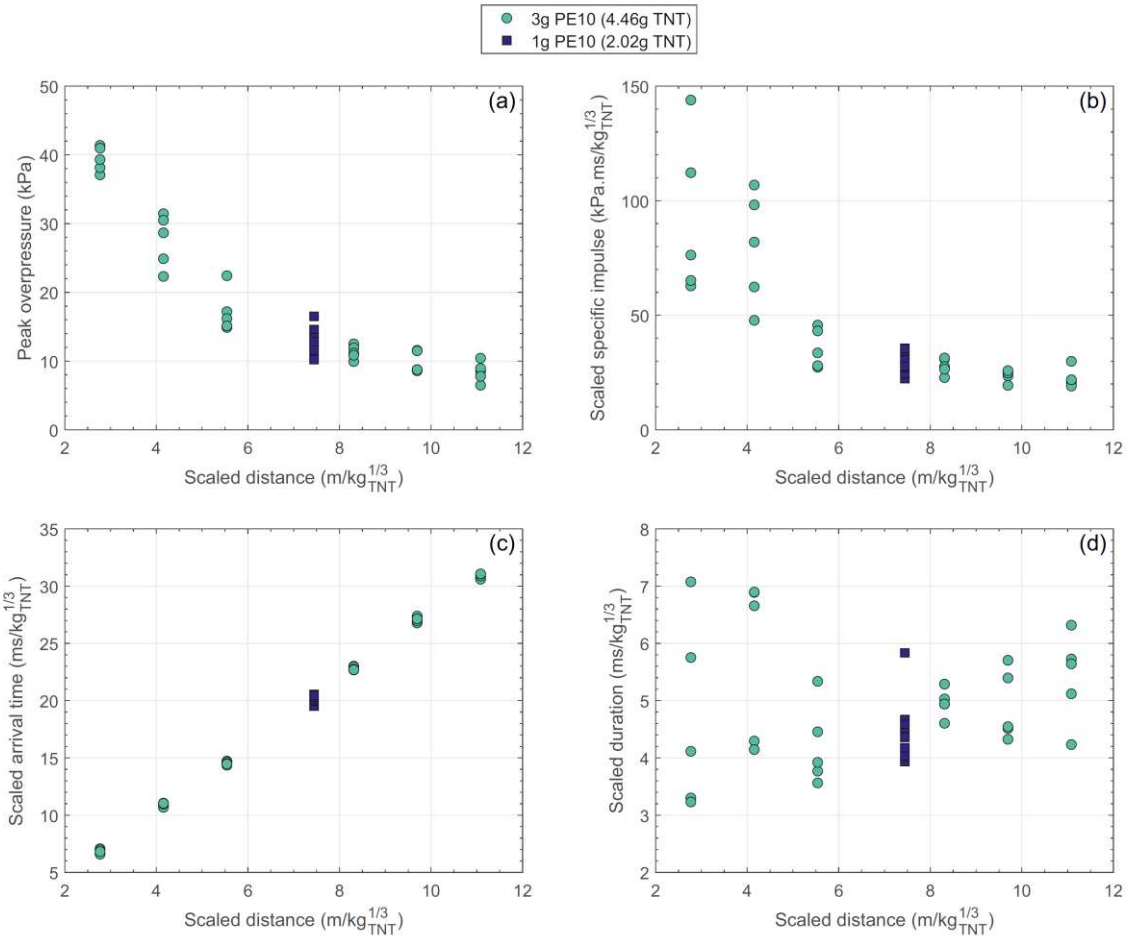

Figure 2. Secondary shock parameters versus scaled distance. (a) Peak overpressure, (b) Scaled specific impulse, (c) Scaled arrival time, (d) Scaled duration.

Predicting the Secondary Shock

A new method for predicting the secondary shock is outlined in Ref. [11]. Briefly, the method calibrates the dummy charge mass and arrival time correction using Monte Carlo sampling of experimental data, with the resulting parameters forming the predictive model. The new loading history is then generated by combining existing UFC positive and negative phase predictions [14] with an additional loading history from this dummy charge mass, as shown in Figure 3.

The process for determining c and dt_{lag} is:

1. For each datapoint, randomly apply statistical noise to experimental parameters (charge mass, stand-off distance), and measurements (peak secondary shock overpressure and secondary shock arrival time).
2. Given a sampled value of peak overpressure, determine the scaled distance which would result in that peak overpressure.

3. Use the sampled stand-off distance to calculate dummy charge mass and, by dividing through by the sampled charge mass, calculate c.
4. Calculate arrival time using a charge mass of cW, and subtract this from the sampled arrival time to calculate dt_{lag}.
5. Repeat for a given number of samples (in this case, 200 samples per datapoint), and repeat for all datapoints.

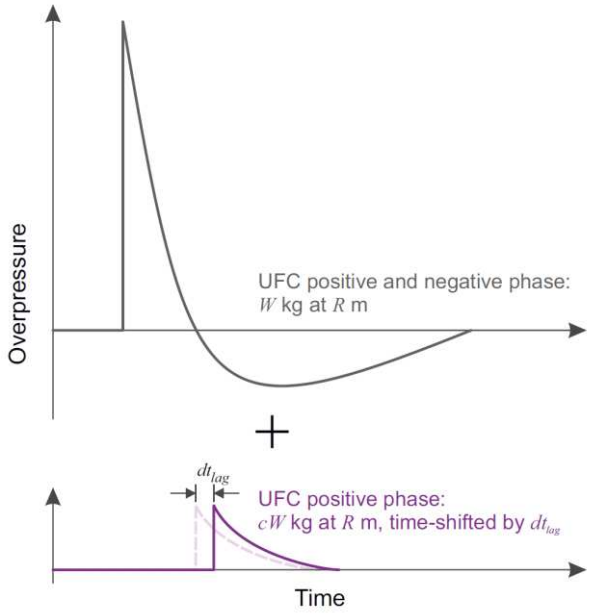

Figure 3. New method for modelling the secondary shock based on superposition of UFC predictions (positive and negative phase) for the original charge mass, W, with loading from a dummy charge mass, cW.

Experimental input parameters were deemed to vary uniformly within the limits with which each parameter could be accurately measured, namely ±1 mg for charge mass and ±3 mm for stand-off distance. Peak pressure was deemed to vary normally with a standard deviation of 0.7 kPa, as determined from the pre-arrival pressure traces in Ref. [11], and arrival time was deemed to vary uniformly up to 50 µs above the measured value on account of how this parameter was determined from the pressure traces (namely, it was given as the *start* of the pressure rise, when feasibly it could have occurred any time between this point and the point of peak pressure, which was usually around a 50 µs window). These statistical distributions are shown in Figure 4.

The reason for evaluating c and dt_{lag} for different charge masses is justified with reference to Figure 5. Here, reflected pressure histories from 4 tests using 250 g PE10 at 5 m stand-off distance (a) are compared against all 11 tests using 1 g PE10 at 0.941 m (b). Scaled distance is effectively the same for both cases, however a clear difference in secondary shock arrival time is observed. This may be evidence of some scale-dependency in secondary shock delay parameters, however this would go against observations presented in Ref. [9]. Instead, it is suggested that this behaviour is most likely due to the large proportion of *other* explosive types in the 1 g charge: it is effectively a 60:40 mix of PE10 and the detonator, in terms of TNT-equivalent NEQ, whereas the 250 g charge is almost entirely PE10.

As a side note, the fact that all 11 tests in Figure 5(b) form such a tight grouping suggests that the high degree of test-to-test consistency seen in larger scale testing [15] can also be replicated at much smaller scale.

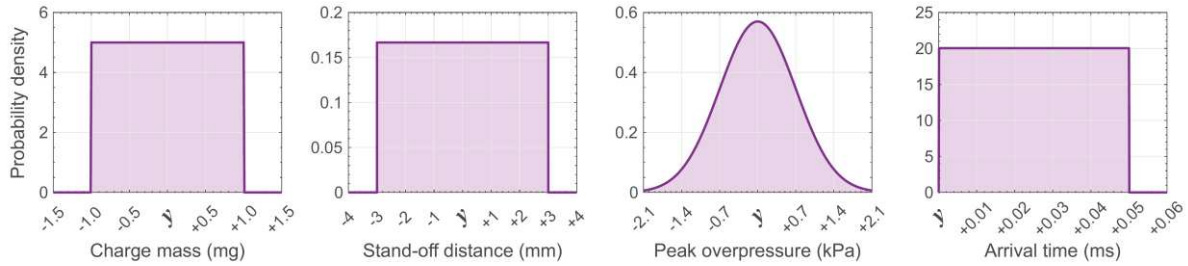

Figure 4. Statistical parameter distributions for Monte Carlo analysis. $\boldsymbol{y}$ denotes the experimental parameters (charge mass, stand-off distance) or measurements (peak overpressure, arrival time).

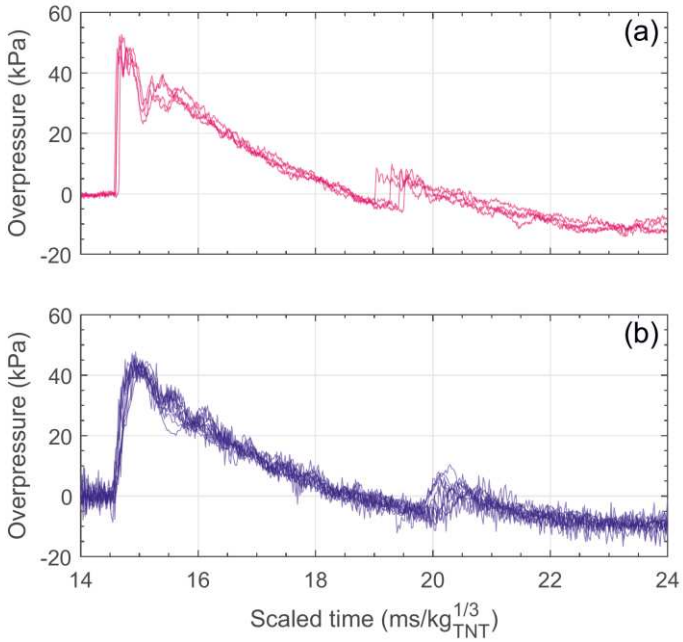

Figure 5. Comparison of results from 250 g PE10 at 5 m (a: 4 tests overlain) and 1 g PE10 at 0.941 m (b: 11 tests overlain) showing clear differences in secondary shock arrival time.

Derived Model Parameters

Results from the Monte Carlo analysis of the 1 g and 3 g tests are shown in Figure 6. Mean, median, and modes of the histograms are provided in Table 2. It can be seen that three of the four distributions are symmetrical and non-skewed and are therefore normally distributed. The exception is the 3 g charge mass multiplier histogram, Figure 6(b), which has a relatively large degree of positive skew and a mode considerably lower than the median, which itself is lower than the mean (albeit to a lesser degree). This may be in part due to some degree of scaled distance dependency of c.

Although the dummy charge mass determined from the larger-scale data in Ref [11] was shown to be invariant of scaled distance, this dependency cannot yet be discounted for the smaller-scale data, particularly because the histogram for the 1 g charges in Figure 6(a), whilst having relatively low variance, was recorded at a single value of scaled distance only. One might expect, therefore, peak secondary shock overpressures in the nearer-field to align better with a smaller value of c (lower peak pressures at a given Z), and the same parameter in the far-field to align better with a larger value of c. How much this is influenced by, or indeed governed by, experimental spread remains to be seen. This idea will be revisited in subsequent sections of this article.

Table 2. Summary of empirical secondary parameters, c and dt_{lag}, determined from 1 g and 3 g PE10 data, compared to existing values for 250 g PE10

PE10 charge mass, W (g)	Charge mass multiplier, c (%)			Scaled time delay, dt_{lag} (ms/kg$_{TNT}^{1/3}$)		
	Mean	Median	Mode	Mean	Median	Mode
1	5.70	5.32	5.0–6.0	1.75	1.72	1.50–1.75
3	5.59	5.00	3.0–4.0	1.82	1.82	1.75–2.00
250	5.40	4.90	4.0–4.5	0.90	0.88	0.80–1.00

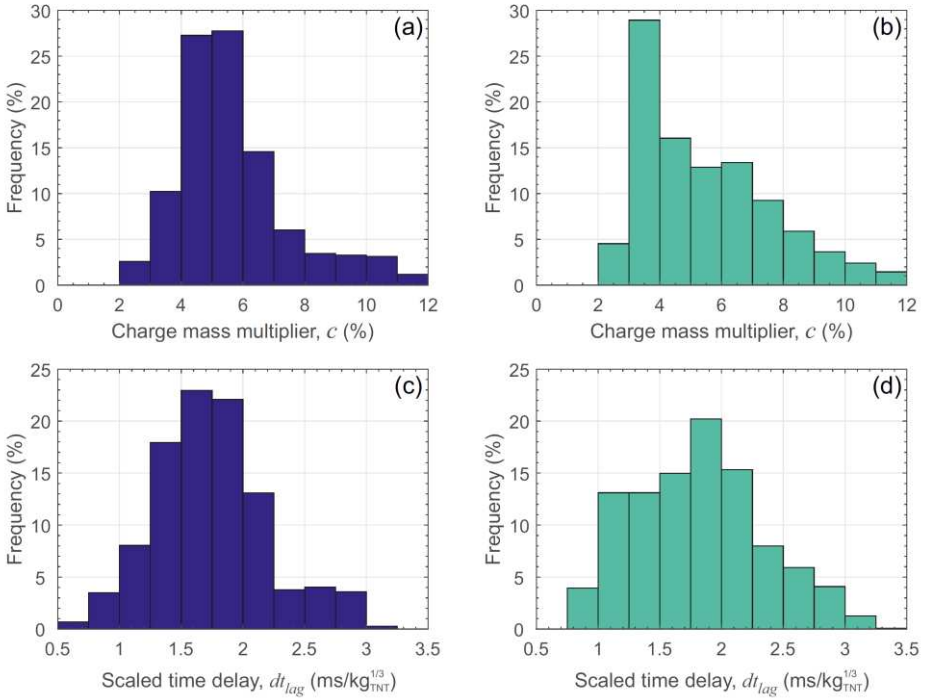

Figure 6. Outputs from the Monte Carlo analysis for determining charge mass multiplier (a, b) and scaled time delay (c, d). Results for 1 g PE10 (a, c) and 3 g PE10 (b, d).

In summary, values of charge mass multiplier $c = 5.5\%$ and scaled time delay $dt_{lag} = 1.75$ ms/kg$_{TNT}^{1/3}$ are deemed appropriate for both 1 g and 3 g PE10 charges.

Results and Discussion

Figure 7 show pressure-time (a) and impulse-time (b) histories for all 5 tests with 3 g PE10 at 1.368 m stand-off distance. Also shown are the UFC positive and negative phase predictions from 4.46 g TNT (dashed black line), as well as the new model predictions formed by superimposing the UFC predictions with an additional loading from 0.223 g TNT ($c = 5.5\%$) at the same stand-off distance, but translated in time by +0.305 ms ($dt_{lag} = 1.75$ ms/kg$_{TNT}^{1/3}$).

It can be seen that the new model offers a considerable improvement on both the form of the pressure history, as well as the net, or final, specific impulse. For this parameter, the experimental values vary between 1.98–4.13 kPa.ms, with a mean value of 2.68 kPa.ms (or 2.32 kPa.ms neglecting the largest value which is out-of-line with the remainder and is potentially an outlier). For comparison, the new model predicts a net impulse of 1.69 kPa.ms, which is much closer than the UFC value of 0.05 kPa.ms.

Predictions for peak secondary shock overpressure versus scaled distance are shown in Figure 8, and are compared against the experimental data. A good level of agreement is achieved throughout, with the exception of the $Z = 2.77$ m/kg$_{TNT}^{1/3}$ data for $W = 3$ g PE10, which all appear below the curve, and the $Z = 11.08$ m/kg$_{TNT}^{1/3}$ data for $W = 3$ g PE10 which generally appear above the curve. This explains the skewed nature of the histogram in Figure 6(b), with a number of larger values of c required to match the far-field data, and a number of smaller values of c required to match the nearer-field data. Generally, however, the method has achieved a high degree of accuracy and its validity has now been proven for over three orders of magnitude variation in charge mass. Note that some signals became corrupted in the later stages of the negative phase, meaning that a comprehensive comparison of net impulses from the entire dataset is not possible for the small-scale test series presented herein.

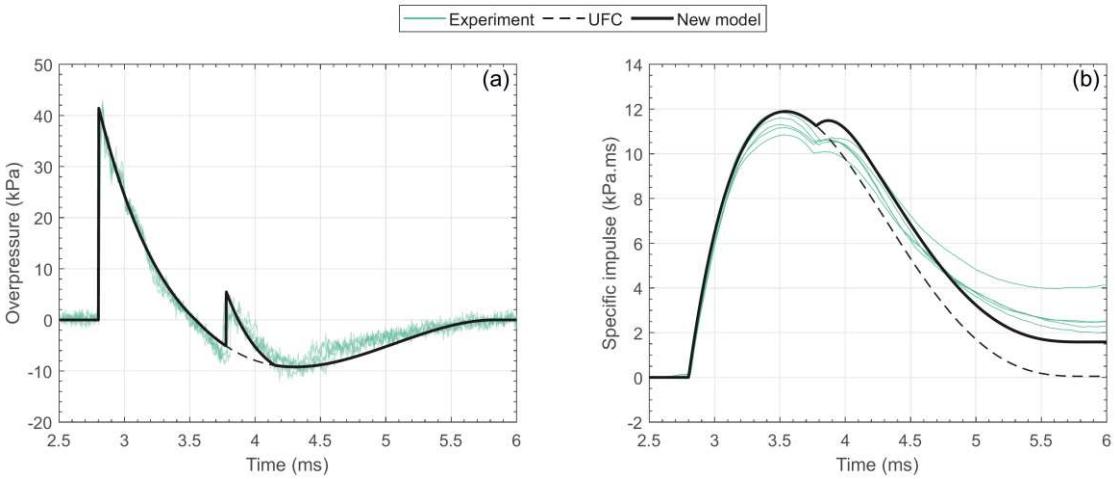

Figure 7. UFC and new model predictions against experimental results (a: Overpressure, b: Specific impulse) for 3 g PE10 at 1.368 m stand-off distance ($Z = 8.31$ m/kg$_{TNT}^{1/3}$, assuming a TNT equivalence of 1.22 [12] and a detonator NEQ of 0.8 g$_{TNT}$; $W_{TNT} = 4.46$ g). 5 tests overlain.

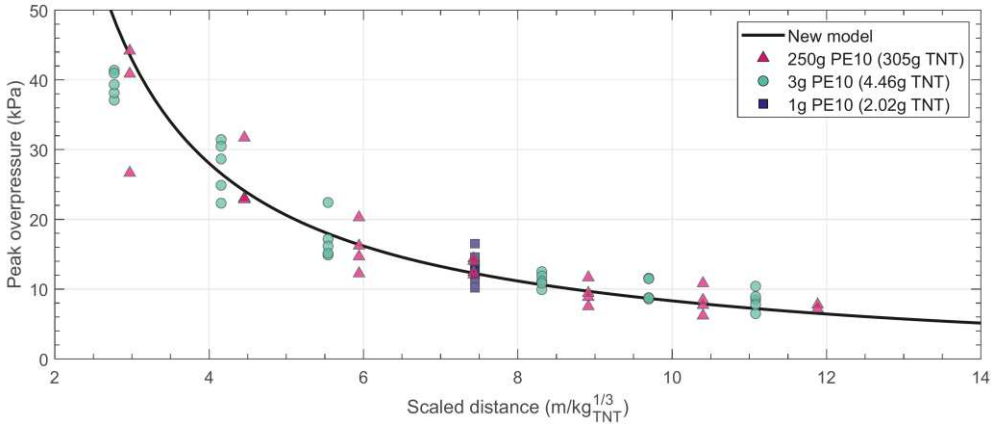

Figure 8. New model predictions for peak secondary shock pressure compared against all experimental datapoints, including larger-scale 250 g PE10 trials [12]. $c = 5.5\%$

High Speed Video Analysis

Figure 9 presents the results from a preliminary analysis using high speed video (HSV) to track the primary and secondary shock fronts. Here, a single test using 250 g PE4 [12] was processed using the method originally proposed in [16] and refined in [17]. Experiments in this series were performed in front of a high-contrast zebraboard (just visible in the top-right corner of Figure 1a), and were filmed

using a Photron SA-Z camera at between 10,000–36,000 frames per second (depending on ambient lighting and field-of-view). This technique allows for distortions in light caused by changes in the refractive index of the propagating shock front to be clearly visible in the recordings (Figure 9(a)).

Various techniques are available to isolate the shock front and quantify its position; in the current work an “image subtraction” technique is applied, where pixel intensity values from the previous frame are subtracted from the current frame, thereby only areas of motion result in a non-zero value and the shock fronts can effectively be isolated (Figure 9(b)). Ultimately, this allows for full-field mapping of the primary and secondary shock fronts as a function of time, as shown in Figure 9(c), where each marker is the average value of the length of a number of radial “spokes” drawn from the centre of the charge (36 in this example, over a 10° wedge). For more details the reader is referred to Ref. [17].

Whilst this technique has not yet been fully explored for the secondary shock, it offers a potential method to study the secondary shock from a large range of charge configurations, including different shapes and compositions. Work is ongoing in this respect.

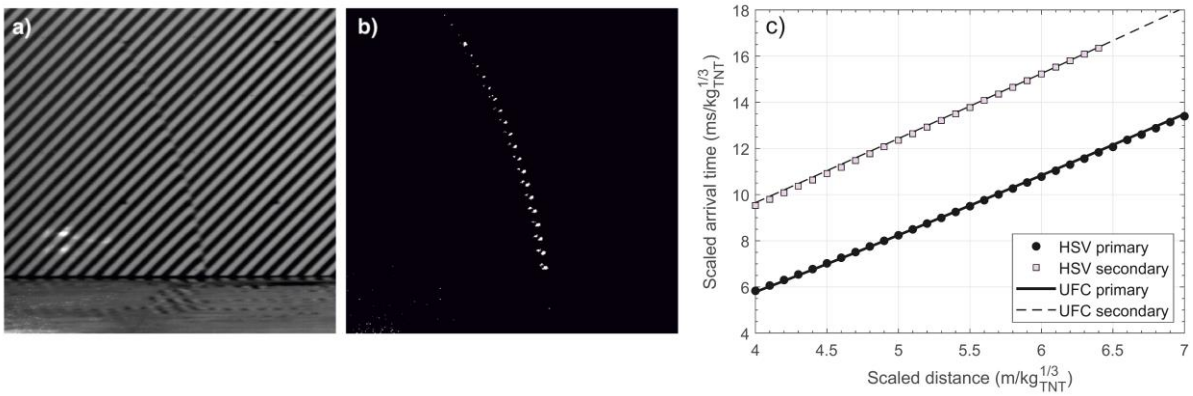

Figure 9. High speed video analysis of the primary and secondary shock. (a) Raw HSV still from a test using 250 g PE4 [12], (b) Shock wave detected using image subtraction, (c) Full-field primary and secondary shock arrival times, with UFC predictions for the secondary shock incorporating values of c and dt_{lag} for PE4 as determined in [11].

Summary and Conclusions

This article presents an overview of a newly-developed method for modelling the often overlooked secondary shock [11]. The model is formed of two parameters: c and dt_{lag} which, respectively, control the magnitude of the secondary shock and adjustments to its arrival time. The resultant loading is given by the superposition of UFC positive and negative phase predictions, and the additional loading pulse from a smaller dummy charge whose properties are controlled by the aforementioned model parameters.

The model has previously been derived from 76 experimental tests using 180–350g of PE4, PE8, and PE10 plastic explosives. In this work, the method is extended to incorporate test data from smaller-scale tests using 1–3g PE10. Monte Carlo sampling is used to incorporate experimental uncertainty in the inputs and measured values, and it was found that values of charge mass multiplier $c = 5.5\%$ and scaled time delay $dt_{lag} = 1.75$ ms/kg$_{TNT}^{1/3}$ represent the secondary shock loading from 1 g and 3 g PE10 charges with a high degree of accuracy. These values compare well to previously-found values of $c = 4.90\%$, derived from tests using 250 g PE10, but the time delay parameter differs considerably from the larger-scale value of $dt_{lag} = 0.88$ ms/kg$_{TNT}^{1/3}$, which may be due to the large proportion of the detonator's NEQ that contributes towards the smaller charge's TNT equivalence.

Some scaled-distance variance was found for c, resulting in a positive skew in the data, however this apparent dependency was not seen in commensurate larger-scale studies and may just be a result of over sensitivity of the method to variations in experimental measurements.

The method has thusfar been calibrated from reflected pressure data from idealised plastic explosives. The use of high speed video analysis has shown promise, and offers the potential to study the secondary shock in a wide variety of settings. Work is ongoing to develop a full predictive model that can incorporate incident pressure data and non-ideal explosive types.

References

[1] LD Sadwin and MM Swisdak Jr. Blast characteristics of 20 and 100 ton hemispherical AN/FO charges. Technical Report *AD871892, NOLTR 70-32*, Naval Ordance Lab, MD, USA, 1970.

[2] JM Dewey. The air velocity in blast waves from t.n.t. explosions. *Proceedings of the Royal Society of London. Series A. Mathematical and Physical Sciences*, **279**(1378):366–385, 1964.

[3] T. Mizukaki, K. Wakabayashi, T. Matsumura, and K. Nakayama. Background-oriented schlieren with natural background for quantitative visualization of open-air explosions. *Shock Waves*, **24**(1):69–78, 2014.

[4] JE Hatfield, GL Pezzola, RE Walker, CS Stephens, and JS Davidson. Fragment response of unreinforced concrete masonry walls subjected to blast loading. *International Journal of Protective Structures*, **1**3(2):161–181, 2022.

[5] T Krauthammer and A Altenberg. Negative phase blast effects on glass panels. *International Journal of Impact Engineering*, **24**(1):1–17, 2000.

[6] M Teich, P Warnstedt, and N Gebbeken. Influence of negative phase loading on cable net facade response. *Journal of Architectural Engineering*, **18**(4):276–284, 2012.

[7] SE Rigby, TJ Lodge, S Alotaibi, AD Barr, SD Clarke, GS Langdon, and A Tyas. Preliminary yield estimation of the 2020 Beirut explosion using video footage from social media. *Shock Waves*, **30**(6):671–675, 2020.

[8] S Rigby and Y Gitterman. Secondary shock delay measurements from explosive trials. In: *Proceedings of the 24th Military Aspects of Blast and Shock (MABS24)*, Halifax, Nova Scotia, Canada, 19–23 September, 2016.

[9] Y Gitterman. Secondary shock features for large surface explosions: Results from the Sayarim Military Range, Israel and other experiments. *Shock Waves*, **24**:267–282, 2014.

[10] L Schwer and S Rigby. Reflected secondary shocks: Some observations using afterburning. In: *Proceedings of the 11th European LS-DYNA Conference*, Salzburg, Austria, 9–11 May, 2017.

[11] SE Rigby, E Mendham, DG Farrimond, EG Pickering, A Tyas, and G Pezzola. An empirical method for modelling the secondary shock from high explosives in the far-field. *Shock Waves* **35**:1–16, 2024.

[12] DG Farrimond, S Woolford, A Tyas, SE Rigby, SD Clarke, A Barr, M Whittaker, and DJ Pope. Far-field positive phase blast parameter characterisation of RDX and PETN based explosives. *International Journal of Protective Structures*, **15**(1):141–165, 2024.

[13] DG Farrimond, A Ratcliff, A Dennis, S Rigby, A Tyas, S Clarke, T Lodge, and W Tolman. Microblast – a benchmarking study of gramme-scale explosive trials. In: *Proceedings of the 26th Military Aspects of Blast and Shock (MABS26)*, Wollongong, Australia, 4–8 December, 2023.

[14] US Department of Defence. *Structures to resist the effects of accidental explosions*. US DoD, Washington DC, USA, UFC 3-340-02, 2008.

[15] SE Rigby, A Tyas, SD Fay, SD Clarke, and JA Warren. Validation of semi-empirical blast pressure predictions for far field explosions – is there inherent variability in blast wave parameters? In: *Proceedings of the 6th International Conference on Protection of Structures Against Hazards (PSH14)*, Tianjin, China, 16–17 October, 2014.

[16] SE Rigby, R Knighton, SD Clarke, and A Tyas. Reflected near-field blast pressure measurements using high speed video. *Experimental Mechanics* **60**(7):875–888, 2020

[17] DG Farrimond, SE Rigby, SD Clarke, and A Tyas. Time of arrival as a diagnostic for far-field high explosive blast waves. *International Journal of Protective Structures* **13**(2):379–402, 2022